

Convective transport in the scrape-off layer of tokamaks

A. Y. Aydemir

Institute for Fusion Studies, The University of Texas at Austin, Austin, Texas 78712

(Received 22 October 2004; accepted 11 April 2005; published online 26 May 2005)

A detailed study of blob formation, dynamics, and the associated convective transport in the scrape-off layer (SOL) of tokamak plasmas is presented. Dissipation level in the system, in addition to the blob size, is shown to play an important role in determining whether a blob propagates as a coherent object. Nonlinear SOL interchange/ballooning modes are shown to be capable of creating blobs near the separatrix without relying on the core or edge-plasma dynamics. Finally, the SOL density profiles under diffusive and convective transport assumptions are compared. In the convective regime, here assumed to be driven by the SOL interchange modes, two different scaling with the machine size R is found for the characteristic density “ e -folding” length λ_n . When the dominant loss mechanism for the blobs is diffusive, the scale length becomes independent of machine size as the connection length increases. In the less typical case where the parallel losses along the open field lines dominate, $\lambda_n \sim R^{1/2}$. © 2005 American Institute of Physics.

[DOI: 10.1063/1.1927539]

I. INTRODUCTION

Highly turbulent nature of the tokamak edge plasmas has been known from the very beginning.¹ More recently it has been recognized that transport in this region, rather than being dominated by diffusive processes, is mostly convective and intermittent (See, for example, Terry *et al.*,² and the references therein). Particles that cross the last closed flux surface (or the separatrix) and enter the scrape-off layer (SOL) with its open field lines are normally expected to follow the field lines to the divertor chamber. However, if the radial convection rate is fast enough, as it is to experimentally observed, particles can recycle at the main chamber wall instead, reducing divertor efficiency and possibly circumventing all together the effectiveness of some elaborate divertor designs. Rapid convective transport of the SOL plasma to the main chamber wall presumably also contributes to increased impurity levels and to observed density limits.

Recently, a possible theoretical explanation has begun to emerge that attributes the radial convective transport in the SOL to formation and propagation of long-lived macroscopic coherent structures, usually referred to as “blobs.” Blobs, typically a few centimeters across, are seen to form near the separatrix and propagate mostly radially, at speeds approaching 1 km/s. There does not appear to be a generally accepted mechanism for their formation. However, a reasonably clear picture of their dynamics and stability have been formulated in a recent series of theoretical and computational studies.^{3–9} The basic mechanism behind the rapid convection appears to be the following: In general, any macroscopic clump of particles in a toroidal plasma would tend to be polarized due to species-dependent processes such as the grad- B and curvature drifts. In the core plasma with its closed flux surfaces, this charge separation is short circuited by free-streaming electrons. In the SOL, however, a finite potential can be supported on the open fields due to sheath formation at the end points. Poloidal electric field thus formed, coupled with the

toroidal magnetic field, then leads to a rapid radial $\mathbf{E} \times \mathbf{B}$ drift of the blob.

Dynamics of blobs have been explored in some detail by D’Ippolito and Myra,⁷ and Yu and Krasheninnikov,⁶ who suggested the existence of an optimum size for a blob to survive as a coherent structure. As first mentioned by Bian *et al.*,⁵ however, radially blobs behave like shock-wave solutions of the Burgers’ equation,¹⁰ where steepening of a propagating front due to nonlinear convection is balanced by diffusion. Therefore, in addition to the size of the blob, dissipation level in the system is expected to play an important role in determining whether a blob is convected as a coherent object. An examination of the role of dissipation in the long-time evolution of blobs is one of the goals of this work.

A related goal is to suggest a simple mechanism for blob creation in the SOL plasma, essentially independent of the core or edge plasma dynamics. It has been known for some time now that the ability of the open field lines in the SOL to support a finite potential, coupled with toroidal curvature, can drive interchange modes on the low-field side of a torus.^{11,12} In numerical calculations, we demonstrate clearly how this mode transforms nonlinearly into “streamers” or “fingers” that detach from the SOL plasma near the separatrix and form independent blobs. Since this process requires not much more than the open field lines of the SOL, it could be a universal mechanism for blob generation.

Role of convective transport in determining the SOL profiles is also another important topic because of its intimate connection with the divertor efficiency and main-chamber recycling issues. Using a power-law distribution for blob sizes and doing an ensemble average over it, D’Ippolito *et al.*⁴ obtained a SOL density e -folding length λ_n that can be shown to scale as $\lambda_n \sim R^{1/3}$, where R is a measure of the machine size (major radius). This scaling is quite different from $\lambda_n \sim R^1$ that one would get from simple ballistic propagation arguments. In a more recent work, Ghendrih *et al.*,¹³ using an elaborate scaling argument based on SOL inter-

change modes, apparently supported by extensive numerical calculations, got a somewhat different result where $\lambda_n \sim R^{5/8}$. But in this work losses but not the curvature drive for the modes seems to have been scaled with R (in our model equations presented below, this incomplete scaling would correspond to varying the parameter $\alpha=2\rho_s/qR$ while holding $\beta=2\rho_s/R$ fixed.) If both effects had been taken into account, their arguments would have led to, ignoring a possibly spurious factor of $1/8$, $\lambda_n \sim R^0$. Here we reexamine this problem assuming, like Ghendrih *et al.*, SOL interchange mode-driven convective transport. Using rigorous arguments, supported by numerical computations, we show that in the limit where the perpendicular particle diffusion dominates over the parallel losses along the open field lines (the most likely regime), the length scale becomes asymptotically independent of the machine size.

In the following section, we present the model equations used throughout this work and discuss some of their consequences.

II. GEOMETRY AND MODEL EQUATIONS

A slab geometry is used in this work, with the mapping $(r, \theta, \zeta) \rightarrow (x, y, z)$, where r, θ, ζ are the radial, poloidal, and toroidal directions, respectively, of a toroidal coordinate system. Model equations describing blob dynamics in the scrape-off layer have been discussed by a number of authors.^{3-5,8,14} With small variations, they are all structurally similar to the isothermal and electrostatic limit of the high- β reduced magnetohydrodynamic equations.¹⁵ We will use the following set, written here in dimensionless form:

$$\frac{\partial U}{\partial t} + [\phi, U] = \alpha\phi - \beta[x, \ln n] + \mu\nabla_{\perp}^2 U, \quad (1)$$

$$\frac{\partial n}{\partial t} + [\phi, n] = -\alpha n + D\nabla_{\perp}^2 n, \quad (2)$$

where $U = \nabla_{\perp}^2 \phi$ is the vorticity and the brackets are defined by $[\phi, U] \equiv \mathbf{z} \cdot \nabla_{\perp} \phi \times \nabla_{\perp} U$. The lengths are measured in units of $\rho_s = c_s/\Omega_i$, where $c_s = \sqrt{kT_e/m_i}$ is the ion acoustic speed, and Ω_i is the ion gyrofrequency. Time is normalized to Ω_i^{-1} . The terms with $\alpha \equiv 2\rho_s/L$, where $L = qR$ (the connection length in the SOL), arise from integrals along the field lines of the parallel divergence of the parallel current (in the vorticity equation) and parallel particle flux (in the continuity equation), respectively. The term with the parameter $\beta \equiv 2\rho_s/R$, which represents the toroidal curvature, is responsible for the polarization of the blob.

A. Analytic solution

Ignoring the parallel loss and perpendicular diffusion terms in the continuity equation [Eq. (2)] and looking for “traveling wave” solutions of the form

$$n(x, y, t) = n(x - V_x t, y), \quad (3)$$

where V_x is a constant radial propagation speed, we obtain $[yV_x + \phi, n] = 0$ or $yV_x + \phi = h(n)$, where $h(n)$ is an arbitrary function of the density. Substituting for ϕ in the vorticity

equation (without the viscosity term) then leads to

$$\alpha h(n) = [h, \nabla_{\perp}^2 h] + \beta \frac{\partial}{\partial y} \left(\frac{\alpha V_x y^2}{2\beta} + \ln n(\xi, y) \right), \quad (4)$$

where $\xi \equiv x - V_x t$. Now if we assume that the density $n(\xi, y)$ is an even function of the poloidal coordinate y , simple symmetry arguments lead to $h(n) = 0$ or

$$\phi + yV_x = 0. \quad (5)$$

Then the remaining terms in Eq. (4) simply give

$$n(\xi, y) = n_0(\xi) \exp\left(-\frac{\alpha V_x y^2}{2\beta}\right), \quad (6)$$

which is of course the separable solution found by Krasheninnikov.³ If the blob has a finite width δ_y , i.e., $n \sim \exp(-y^2/\delta_y^2)$, Eq. (6) leads to the well-known result

$$V_x = 2 \frac{\beta/\alpha}{\delta_y^2}. \quad (7)$$

In other words, smaller blobs have higher convection velocities.

The uniqueness and generality of the solution in Eq. (6) do not appear to have been appreciated in the literature. Recall that we arrived at it by making only two assumptions: (i) the solution has the form of a traveling wave, $n = n(x - V_x t, y)$, and (ii) it is even in y , a common (but not universal) feature of the blobs studied in the literature. In particular, we did not *a priori* ignore inertia, represented by the $[h, \nabla_{\perp}^2 h]$ term in Eq. (4). The fact that the inertia term vanishes (because $h=0$) is part of the solution, not one of the assumptions. Thus, we conclude that there can be no other even solutions in the form of a traveling wave that somehow include finite inertia, and the one given above is the most general one possible that is consistent with our two assumptions.

Symmetry arguments alone cannot rule out immediately solutions with odd poloidal symmetry. However, if they exist, such solutions would represent not blobs but a “blob-hole” pair and be physically meaningful only if $n_0 \gg |n_b|$, where n_0 is the background SOL density and n_b is the blob or hole density. Using symmetry arguments again, we can show that holes (density depressions) and blobs are convected radially in opposite directions. Thus, the pair would have an odd convection velocity and violate our assumption of constant V_x . In summary, there are no odd solutions consistent with our assumptions, and the one in Eq. (6) is the only even solution possible. Of course, general solutions without any symmetries cannot be ruled out on the basis of these symmetry arguments.

Before moving on to a discussion of the numerical solutions in the following sections, we will point out a couple of important differences between the exact analytic solution given above and the computational results. First, we do find numerical solutions with even symmetry that have a finite inertia term. Thus, these must differ from our simple analytic solution in a fundamental way. Since the only assumption leading to Eq. (4) was $n = n(x - V_x t, y)$, with a constant convection velocity V_x , this traveling-wave assumption must not

be valid in general, even when the blobs behave as “coherent structures.” A second problem is that the solution for the potential, $\phi = -yV_x$, does not satisfy any reasonable boundary conditions in either radial or poloidal directions. It merely extends the electric field in the blob uniformly throughout the SOL, which is not physical. A potential that is radially uniform ($\partial\phi/\partial x = 0$) is also inconsistent with the presence of a wall at some point $x = x_{\text{wall}}$, where presumably ϕ would have to vanish. In numerical solutions with either homogeneous Dirichlet or Neumann boundary conditions at the poloidal boundaries, we find that there is a stationary point $y = y_s$ where $V_x(x, y_s) = 0$. Thus, ϕ has a well-defined dipole structure, and the radial convection is necessarily slower near the edges of the blob than at its center. Under suitable conditions, this sheared velocity profile can drive Kelvin–Helmholtz (KH) instabilities.¹⁶ A related process is the nonlinear steepening of the leading edge of the density profile to a shocklike formation.⁵ Therefore, the radial profile of the blobs, when they remain as coherent structures, resembles shock-wave solutions of the Burgers’ equation,¹⁰ but one with a trailing edge that is almost stationary. In short, we will see below that the actual nonlinear dynamics of blobs is, in general, quite complicated and is only superficially like the traveling wave solution of the preceding analytic discussion.

The following section examines the long-time nonlinear evolution of blobs of various sizes and looks at the effects of dissipation on the dynamics.

III. BLOB DYNAMICS

Dynamics of individual blobs have been examined in some detail in previous theoretical and computational studies.^{6,7} In this section, we will briefly summarize our results, which, for the most part, confirm the findings of previous workers. Some differences observed here, especially in the long-time evolution of the blobs, will be pointed out in appropriate places.

For the sake of completeness, we start with a discussion of the relevant characteristic length and time scales in the problem. If we rescale the dependent and independent variables as $x \rightarrow a_0 x$, $t \rightarrow t_0 t$, $\phi \rightarrow \phi_0 \phi$, $n \rightarrow n_0 n$, and use $v_0 = \phi_0/a_0$ and $t_0 = a_0/v_0$, we can easily show the following.

- (1) Inertia is not important if $a_0^5 \gg \beta/\alpha^2$. In dimensional units, this condition defines an inertial length scale

$$a_m = \rho_s \left(\frac{L^2}{2\rho_s R} \right)^{1/5}, \quad (8)$$

above which inertia does not play an important role in the coherent dynamics of blobs. However, as we will see below, large blobs may be unstable to modes with wavelengths shorter than the blob dimensions, thus again elevating the relevance of inertia.

- (2) Viscosity diffusion is not important (in comparison to other terms on the right-hand side of the vorticity equation) if $a_0^4 \gg \mu/\alpha$. In dimensional units, this condition defines a viscosity length scale.

$$a_\mu = \rho_s \left(\frac{\mu L}{2\Omega_i \rho_s^3} \right)^{1/4}, \quad (9)$$

above which the diffusion term is not important. If we assume $\mu \sim D \sim 1 \text{ m}^2/\text{s}$, this condition is easily satisfied for blob sizes greater than a few ρ_s .

- (3) In the density equation, particle losses due to free-streaming along the field lines is not important if $a_0^3 \ll (\beta/\alpha^2)$. Again in dimensional units, this condition defines a parallel loss length scale

$$a_L = \rho_s \left(\frac{L^2}{2\rho_s R} \right)^{1/3}, \quad (10)$$

below which perpendicular convection dominates over the parallel losses.

- (4) Finally, particle density diffusion is not important (compared to the left-hand side of the density equation) for $a_0 < \beta/(\alpha D)$, defining a particle diffusion length scale

$$a_D = \frac{L\Omega_i \rho_s^3}{RD}. \quad (11)$$

Below this scale, which is too large to be relevant to the present discussion, convection dominates over diffusion. This counterintuitive existence of an upper bound on blob size here is due to the fact that the characteristic time scale for blob dynamics, $t_0 = a_0/v_0$, is cubic in a_0 , whereas the diffusion time $t_D = a_0^2/D$ is only quadratic.

Using $c_s = 6 \times 10^4 \text{ m/s}$, $\Omega_i = 10^8 \text{ s}^{-1}$, $L = 40 \text{ m}$, and $R = 2 \text{ m}$ (similar to the parameters used by Yu and Krasheninnikov⁶), we get $\alpha = 3 \times 10^{-5}$, and $\beta = 6 \times 10^{-4}$. These lead to the following dimensionless length scales (in units of $\rho_s = 6 \times 10^{-4} \text{ m}$):

$$a_m = 15, \quad a_\mu = 3,$$

$$a_L = 87, \quad a_D = 7.2 \times 10^3,$$

where we also assumed $\mu = D = 0.1 \text{ m}^2/\text{s}$. In this part of the work (blob dynamics), we will ensure that the blob size is larger than the viscous dissipation scale length, $\delta_b > a_\mu$. Also, unless otherwise noted, we will ignore the parallel particle loss term in the continuity equation; thus, the upper bound on blob size will be determined by stability.

In general, for blobs of size $\delta_b < a_m = 15$, inertia will be important, and we would expect KH modes to play a dominant role in their nonlinear evolution. In the opposite limit, $\delta_b \gg a_m$, we will see that interchange modes become significant. Thus, only blobs with $\delta_b \sim a_m$ are expected to survive as coherent structures and contribute significantly to the convective transport in the SOL. However, within this general pattern, we will see that the particle and vorticity diffusion rates will play an important role also.

A. Small blobs

For $\delta_b \ll a_m$, rapid convection ($V_x \sim 1/\delta_b^2$) and the velocity shear that accompanies it lead to formation of Kelvin–Helmholtz vortices and vortex shedding (also referred to as “KH rollup”). As a result, small blobs do not survive as

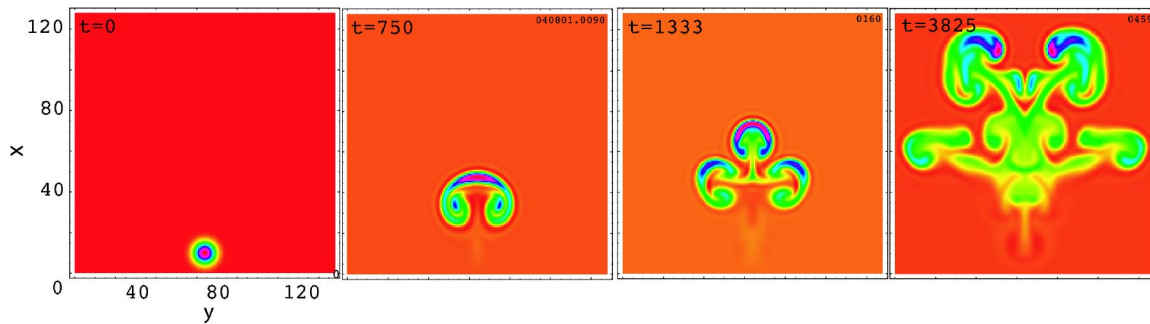


FIG. 1. (Color online). Nonlinear evolution of a small blob ($\delta_b=5$). In this and the following figures, the bottom boundary represents the separatrix (or the last closed flux surface). The horizontal and vertical coordinates are the poloidal and radial directions, respectively. The lengths shown are in units of $\rho_s = 0.06$ cm. Time is normalized to $\Omega_i^{-1} = 1 \times 10^{-8}$ s. Thus, for the last frame, $t = 38.25 \mu\text{s}$. The relevant dimensionless parameters are $\alpha = 3 \times 10^{-5}$, $\beta = 6 \times 10^{-4}$, $\mu = D = 2 \times 10^{-3}$.

coherent structures. A highly complicated (but typical) dynamical evolution is shown in Fig. 1 for a blob of size $\delta_b = 5$ (blob radius = 0.3 cm). Unless otherwise stated, we will use in this section a constant background SOL density of $n_0 = 1$, peak blob density of $n_b = 10$, and the dimensionless parameters $\alpha = 2 \times 10^{-5}$, $\beta = 6 \times 10^{-4}$. For this particular calculation, we also had in dimensionless units $\mu = D = 2 \times 10^{-3}$ (or $0.07 \text{ m}^2/\text{s}$). It is clear that, although the process is entirely convective, the end result is turbulent particle diffusion in both poloidal and radial directions, with the original mass in the blob getting dispersed over a large section of the poloidal plane ($\approx 7 \times 7 \text{ cm}^2$). Note that short-time calculations in the literature, which typically terminate at a point corresponding to $t = 750$ in Fig. 1, give the misleading impression of coherence for blobs of this size.

B. Large blobs

Large, slow-moving blobs are not affected by Kelvin–Helmholtz modes. Nevertheless, they do not remain as coherent objects, because they tend to be unstable to interchange modes.^{6,7,11,12} A dramatic example of the “Rayleigh–Taylor fingers” that develop under these conditions is shown in Fig. 2, where $\delta_b = 60 \gg a_m$. In these long-time calculations,

the original fingers themselves bifurcate and break up the blob into smaller pieces, again dispersing its content over a large area. This complex dynamical behavior is missed when inertia is ignored or if the evolution is not followed long enough in time. Note that the drive for the interchange modes responsible for the fingers is size independent; it is not seen for small blobs because it tends to be preempted by the faster-growing KH modes.

C. Coherent blobs and the role of dissipation

The results of the preceding sections, which showed that neither the small ($\delta_b \ll a_m$) nor the large ($\delta_b \gg a_m$) blobs remain as coherent structures, suggest that there might be a blob size, presumably $\delta_b \sim a_m$, that would guarantee coherence. In fact this appears to be the conclusion of a number of previous works on this topic.^{6,7} We find that coherence is closely connected not only with the size of the blob but also with the amount of dissipation in the system, i.e., the viscous diffusion in the vorticity equation [Eq. (1)], and the particle diffusion in the continuity equation [Eq. (2)]. For low dissipation, for example, with $\mu = D = 2 \times 10^{-3}$ in dimensionless units ($0.07 \text{ m}^2/\text{s}$), a blob of size $\delta_b = 30 = 2a_m$ exhibits only a semicoherent behavior, as seen in Fig. 3. As it moves radi-

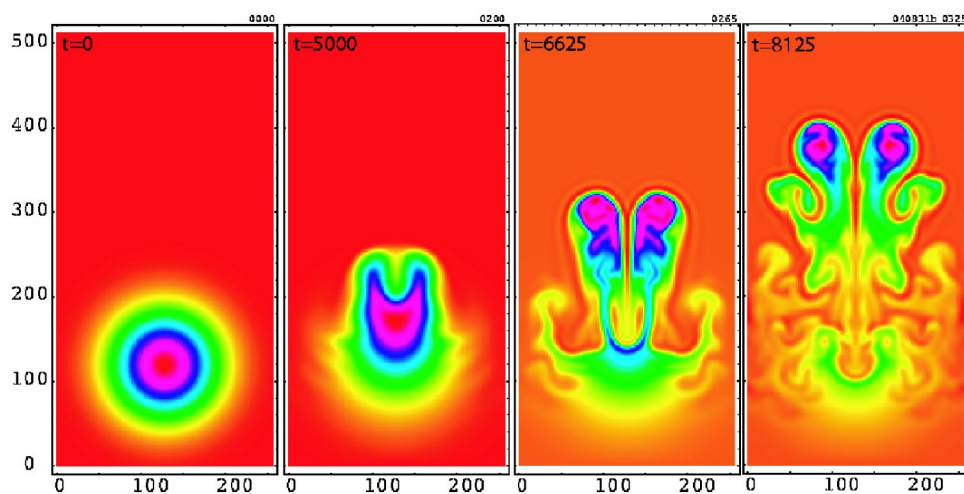


FIG. 2. (Color online). Nonlinear evolution of a large blob of size $\delta_b = 60$. Other parameters are the same as in Fig. 1. Note the development of “Rayleigh–Taylor fingers,” which break up the blob into smaller pieces and effectively disperse the particles over a large area.

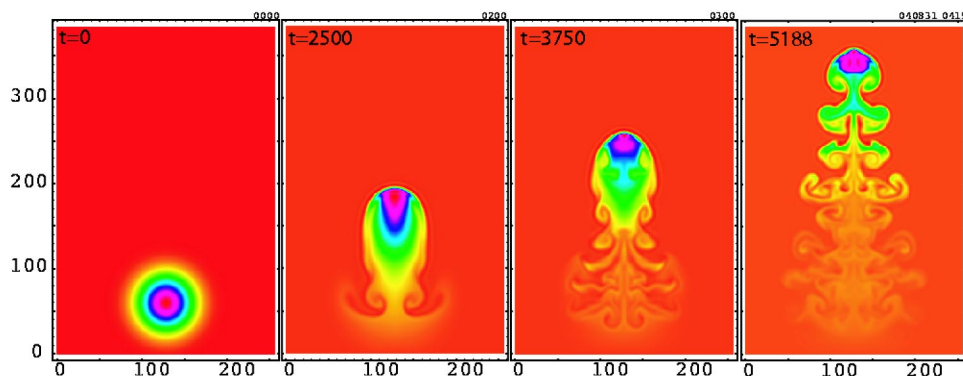


FIG. 3. (Color online). Nonlinear evolution of a blob of size $\delta_b=30$. Other parameters are the same as in Fig. 1. In particular, $\mu=D=2\times 10^{-3}$. This semicoherent blob continually sheds vortices and loses mass.

ally, it continually sheds vortices and loses mass. The whole process feeds on itself; as it gets smaller, the blob moves faster, creating higher flow shear and even more shedding. This vortex shedding, associated with nonlinear KH modes, is a common feature of blobs of a wide range of sizes; under these low-dissipation conditions, we have observed them even for $\delta_b \geq 2a_m$, a point above which the nonlinear dynamics begins to be affected by the interchange mode as well, as seen earlier in Fig. 2. Thus, with low dissipation we do not see strictly coherent behavior for any blob size, and the nonlinear evolution varies continuously between KH induced vortex shedding and finger formation due to interchange modes.

Coherent behavior emerges with higher dissipation in the system. For example, the same blob in Fig. 3 with $\delta_b=30$ propagates as a coherent structure when the coefficients are raised to $\mu=D=2\times 10^{-2}$. Figure 4 shows that now the blob remains essentially intact until it comes in contact with the wall. Note the sharp leading edge and a long tail that are common features of coherent blobs.

The differences between these low- and high-dissipation cases can be understood in terms of the effect of dissipation on the structure of blobs. As mentioned earlier, radial profile of a propagating blob resembles “shock-wave” solutions of the Burgers’ equation (Fig. 5), where the steepening effect of the convective nonlinearity is balanced by a second-order diffusion term. Diffusion plays a stabilizing role here by wid-

ening the “shock front” and at the same time reducing the poloidal shear in the convection velocity. Thus, the particle and momentum diffusion contribute in an essential way to the coherence of blobs and should be an integral part of any discussion on their long-term behavior. For reference, with our usual parameter set, coherence emerges only for diffusion coefficients of the order of $1\text{ m}^2/\text{s}$ in our calculations.

Until now we assumed the existence of blobs in the SOL and examined their dynamics under various conditions. We saw that there is a dissipation-dependent optimum blob size, $\delta_b \sim a_m$, that leads to coherent structures. A smaller or larger blob tends to be unstable and break up into smaller pieces, effectively dispersing its contents over an area much larger than its original size. Next we look at a possible mechanism for blob formation in the scrape-off layer.

IV. SCRAPE-OFF LAYER STABILITY AND BLOB CREATION

Special nature of the stability on the open field lines of the SOL has long been recognized and studied in a number of works. Nedospasov¹¹ examined interchange modes driven by toroidal curvature, which was later generalized by Garbet *et al.* to include the effects of polarization currents.¹² Others include Berk and co-workers, who looked at modes driven by electron temperature gradients,^{17,18} and Novakovskii *et*

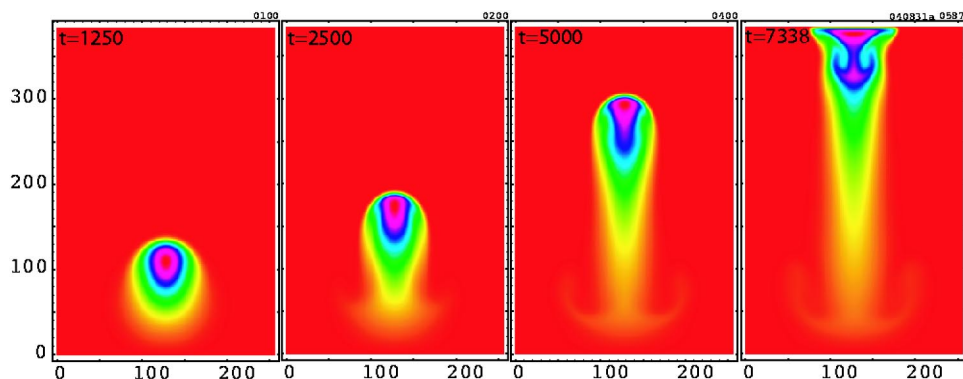


FIG. 4. (Color online). The blob of Fig. 3 with increased dissipation: $\mu=D=2\times 10^{-2}$ ($0.72\text{ m}^2/\text{s}$). Unlike the low-dissipation case, here the blob propagates as a coherent structure. It covers a radial distance of $\approx 19.4\text{ cm}$ in $73.4\text{ }\mu\text{s}$.

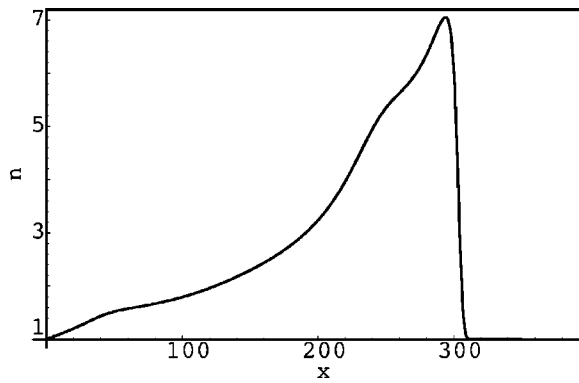


FIG. 5. Radial density profile along the symmetry axis for the third frame (at $t=5000$) of Fig. 4.

*al.*¹⁹ and Kerner *et al.*,²⁰ who examined resistive ballooning and interchange modes, respectively.

It is probably already clear from the discussion in the preceding section that the interchange modes responsible for the break-up of large blobs can play an important role in the stability of the background SOL plasma also. Here we revisit linear stability in the SOL and include the effects of dissipation in our discussion. We assume the density varies as $n_0(x) = \tilde{n}_0 \exp(-x/\lambda_n)$, where λ_n is a measure of the SOL density width, and introduce perturbations of the form $n(x, y, t) = \tilde{n}(x) \exp[-i(\omega t - ky)]$. Then Eqs. (1) and (2) can be linearized to give the following local dispersion relation:

$$(i\omega - \mu k^2)(i\omega - Dk^2) - \frac{\alpha}{k^2}(i\omega - Dk^2) - \frac{\beta}{\lambda_n} = 0, \quad (12)$$

where we assumed $\partial^2/\partial x^2 \ll k^2$ and also ignored the parallel loss term in the density equation. With $\mu = D = 0$, we get

$$\gamma = -\frac{\alpha}{2k^2} + \left[\frac{\beta}{\lambda_n} + \left(\frac{\alpha}{2k^2} \right)^2 \right]^{1/2}. \quad (13)$$

The maximum growth rate is $\gamma_{\max} = \sqrt{\beta/\lambda_n}$ (for $k \rightarrow \infty$), which can also be extracted from the results of Ref. 6. Note that when the polarization current is ignored, as in Refs. 7 and 11, a growth rate that scales as $\gamma \sim k^2$ is obtained, which is quite different from Eq. (13). When dissipation is included, there is a k_{\max} such that modes with $k > k_{\max}$ are stable. However, this cutoff in k requires both coefficients μ and D to be finite. Note also that, although this is a flute interchange mode (constant along the field lines), the curvature drive responsible for it is active only on the outboard side of the torus, giving it also a ballooning character. Thus, a proper treatment would actually require a three-dimensional (3D) calculation, which is beyond the scope of this work.

In the following section, we look at the linear and nonlinear forms of this interchange/ballooning mode numerically and show how it might lead to blob formation.

A. Numerical studies of linear and nonlinear interchange modes in the SOL

In Fig. 6 we plot the growth rate of the interchange mode obtained from the numerical solution of the original model

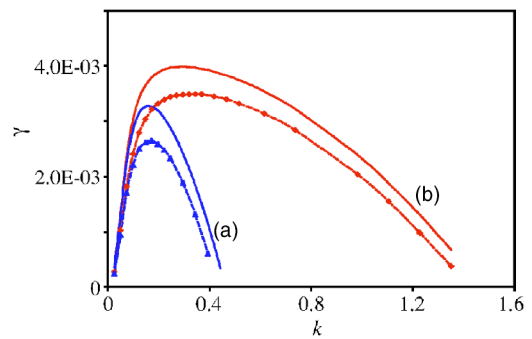


FIG. 6. (Color online). Growth rate of the SOL interchange mode as a function of the poloidal wave number k for two different dissipation rates. (a) High dissipation: $\mu = D = 2 \times 10^{-2}$ (or $0.72 \text{ m}^2/\text{s}$). (b) Low dissipation: $\mu = D = 2 \times 10^{-3}$. In both cases the solid lines are from the local dispersion relation [Eq. (12)], with $\alpha = 3 \times 10^{-5}$, $\beta = 6 \times 10^{-4}$, and $\lambda_n = 32$. The dashed lines are from the numerical solution of Eqs. (1) and (2).

equations [Eqs. (1) and (2)] and compare it with the local dispersion relation, Eq. (12). Numerical results are 10%–15% lower, probably because the dispersion relation underestimates the inertia term by letting $\partial^2/\partial x^2 \rightarrow 0$. As mentioned in the preceding section, dissipation introduces a cutoff wave number k_{\max} above which the mode is stable, and as expected, k_{\max} decreases with increasing dissipation: $k_{\max} \sim \mu^{-1/4}$ assuming $\mu = D$. With our usual parameters, the wavelengths corresponding to the highest growth rate are $\lambda_{\text{low}} \approx 22$, and $\lambda_{\text{high}} \approx 39$ for the low and high-dissipation cases, respectively (in units of ρ_s). Note that both are somewhat larger than the inertial length scale, $a_m = 15$. In particular, λ_{high} is roughly comparable to the size of the blob (its poloidal width) in Fig. 4 that propagates as a coherent structure.

Even in the high-dissipation case, there is a wide range of unstable poloidal mode numbers. In order to avoid the turbulence that would follow the excitation of all these different wavelengths, we introduce a density perturbation with a single wave number $k=0.17$ [at the maximum of the growth-rate curve (a) of Fig. 6] and follow its nonlinear evolution. The results are shown in Fig. 7. The initial symmetry of the $m=7$ mode is preserved (but not artificially enforced) throughout the calculation. The early nonlinear stage in (b) is

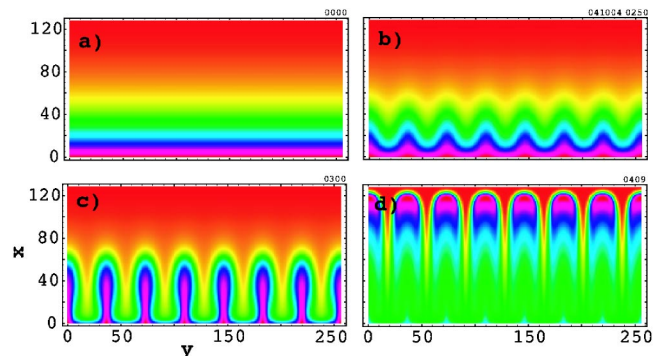


FIG. 7. (Color online). Nonlinear evolution of a single mode ($k=0.17$). (a) The initial state. (b) Early nonlinear stage. (c) Formation of fingers. (d) Fingers have detached from the base at $x=0$, essentially forming independent blobs. See the next figure for the corresponding radial density profiles.

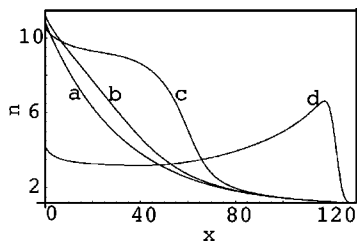


FIG. 8. Radial profile of the density through the center of one of the fingers at times corresponding to the four panels of Fig. 7. Curve (a) shows the initial SOL density profile.

followed by formation of seven “fingers” that eventually detach from the base at $x=0$ [the last closed flux surface (LCFS)] and become essentially seven different blobs. The radial (upward) convection mechanism for the fingers is the same as in the single blobs: the $\mathbf{E} \times \mathbf{B}$ drift, in this case driven by the sinusoidal polarization of the SOL plasma that results from interaction of the density perturbation with the toroidal curvature. Detachment from the LCFS and formation of blobs, with their steepened leading edges, can also be seen in the time history of their density profiles in Fig. 8. Note that, in order to prevent particle flux across the LCFS (from the core plasma into SOL) on the fast, convective time scale of this problem, we imposed the boundary condition $V_x=0$ at $x=0$; thus, there is no radial convection at the $x=0$ surface, and the density drop seen there in Fig. 8 is purely due to particle diffusion. Note also that the continuity equation in the nonlinear calculations of this section is augmented with a source term such that $dn/dt = D\nabla_{\perp}^2[n - n_0(x)]$. Thus, in the absence of any unstable mode activity, there is no diffusion of the background density, i.e., with $\phi=0$, we have $\partial n / \partial t = 0$.

The nonlinear evolution of this periodic, single-mode, perturbation indicates how blob formation might be driven by an interchange/ballooning mode in the SOL plasma. However, single- k perturbations are not very realistic. Next we discuss an example from a series of nonlinear calculations with nonperiodic perturbations of various degrees of localization.

B. Blob creation with localized perturbations

Rather than a sinusoidal perturbation, here we choose one with a Gaussian profile, $\delta n \sim \exp(-[(x/w_x)^2 + (y/w_y)^2])$ to see if isolated blobs can be created with the SOL interchange mode as the sole driving mechanism. A result is shown in Fig. 9, where the emergence of a series of blobs from the nonlinear evolution of the excited modes can be seen. For this particular calculation we used the SOL width $\lambda_n=30$, and the perturbation widths $w_x=w_y=30$. However, the results appear to be independent of w_x, w_y , as long as $w_y \ll L_y$, where L_y is the system size in the poloidal direction.

The panel (a) of the figure shows the initial, poloidally uniform SOL density, $n_0(x) = \bar{n}_0 \exp(-x/\lambda_n)$. The early nonlinear stage in (b) leads to a single blob formation with two smaller sidebands, leaving a density hole behind it. Because of the boundary conditions imposed at the separatrix ($V_x=0$ at $x=0$), the hole does not propagate out of the computa-

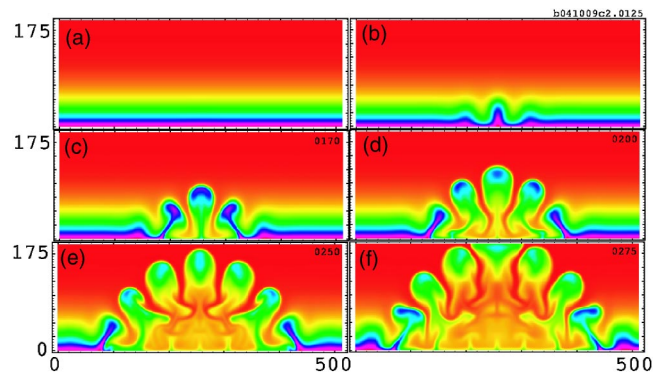


FIG. 9. (Color online). Blob creation with a localized Gaussian perturbation. Note that the perturbation generated by the central blob propagates poloidally in both directions, generating more blobs.

tional domain in the core plasma direction ($x < 0$). However, interacting with the sidebands, it leads to creation of two more blobs [panels (c) and (d)]. Thus, in a cascade, the original perturbation travels outward in both directions along the $x=0$ surface, forming more blobs, until essentially all the particles are evacuated from this area.

Not surprisingly, blob size (the poloidal width δ_y) appears to be determined by the most unstable wavelength in the system, $\lambda_{lin}=39.3$. This correlation between δ_y and λ_{lin} is supported by some simple scaling studies. It can be shown using the dispersion relation Eq. (12) that $\lambda_{lin} = 2\pi(D/\alpha)^{1/4}$ in the limit $\lambda_n \rightarrow \infty$. In agreement with this scaling, in nonlinear calculations where we let $\beta \rightarrow 4\beta$, with little expected change in λ_{lin} , the number of blobs do not vary. In contrast, letting $\alpha \rightarrow 4\alpha$, which leads to $\lambda_{lin} \rightarrow 29.1$, increases the number of blobs roughly by 50%.

Our initial aim here was to produce a single, isolated, blob using a localized perturbation. However, it now looks obvious that under these conditions this goal is not achievable. With a poloidally uniform initial state, there is no mechanism to stop the initial disturbance from propagating along the separatrix; more and more blobs necessarily follow the initial one in an expanding semicircular pattern, as seen in Fig. 9. But under experimental conditions, the SOL plasmas are turbulent, spatially nonuniform, and are replenished by particle flux from the core plasma. Any one of these conditions may interfere with the “blob-proliferation” we see here.

Next we examine how convective transport determines SOL density profiles.

V. THE INTERCHANGE-MODE TURBULENCE AND THE DENSITY PROFILE IN THE SCRAPE-OFF LAYER

If the SOL density profile was determined solely by particle diffusion across the separatrix that is balanced by parallel losses along the open field lines, then the density scale length would be simply, in dimensionless units, $\lambda_{diff} = (D/\alpha)^{1/2}$, a point that will be made explicit in Appendix A. Using $\rho_s=2$ mm, $L=5$ m, $\Omega_i=2.4 \times 10^7$ /s, and $D=0.1$ m²/s (NSTX-like parameters), we would have $\lambda_{diff} \approx \rho_s$, which is obviously much shorter than experimentally observed. Ex-

planation for this apparent discrepancy between the purely diffusive length scale and the observations of nearly “flat” SOL density profiles in tokamaks²¹ requires either an effective diffusivity D_{eff} that is quite large and gets larger in the direction of the wall or a convective mechanism for cross-field particle transport. Blobs (or “fronts”) are assumed to provide a means for the latter.

In this section, we set aside the question of individual blob dynamics and examine the implications of convective transport driven by the SOL interchange/ballooning modes discussed earlier. In particular, we derive a mean density profile that is in good agreement with our numerical calculations.

The physical picture we have in mind here is the following: blobs are continually created near the separatrix and propagate outward. A time and spatial average (over the poloidal coordinate) then determines a mean density profile in the SOL. We start with the following assumptions.

- (1) The blob density and size evolve according to the following equation:

$$\frac{\partial n}{\partial t} + V_x(t) \frac{\partial n}{\partial x} = -an + D\nabla_{\perp}^2 n. \quad (14)$$

- (2) The blob velocity is given by $V_x(t) = 2(\beta/\alpha)/a^2(t)$, where $a(t)$ is the instantaneous blob size [See Eq. (7)].
- (3) The initial blob size is determined by the most unstable wave number $k \approx (\alpha/D)^{1/4}$. Thus, $a_0 = a(t=0) \equiv 2\pi(D/\alpha)^{1/4}$. Nonlinearly developed length scales are somewhat larger; we will see that a_0 needs to be multiplied by a factor of 1.3–2 to get better agreement between nonlinear numerical calculations and the analytic results to be presented. Thus, a_0 will be our only “adjustable parameter,” but adjustments necessary will be less than a factor of 2.
- (4) When they are created (at $x=0$), rather than an ensemble of various sizes, all blobs have approximately the same size a_0 with a Gaussian shape. Thus,

$$n[\xi(t=0), y, t=0] = n_b \exp[-(\xi^2 + y^2)/a_0^2], \quad (15)$$

where $[\xi(t), y]$ is a comoving coordinate system with $\xi(t) \equiv x - \int_0^t V_x(t') dt'$.

- (5) Secondary instabilities such as the Kelvin–Helmholtz or Rayleigh–Taylor modes do not play a role in the dynamics.

Under these assumptions, the blob evolution equation, Eq. (14), has the following simple solution in the (ξ, y) coordinate system:

$$n(\xi, y, t) = n_b \frac{a_0^2}{a^2(t)} \exp[-(\xi^2 + y^2)/a^2(t)] \exp(-at), \quad (16)$$

where $a(t) = (a_0^2 + 4Dt)^{1/2}$ is the instantaneous blob size that increases continuously due to diffusion. As expected, the parallel losses change the amplitude but not the size of the blob.

In order to obtain a mean density profile, we define, at $x=X(\tau)$, where $X(\tau) \equiv \int_0^{\tau} V_x(t') dt'$, the following time and poloidal length-averaged density:

$$\bar{n}[X(\tau)] \equiv \frac{1}{\Delta\tau L_y} \int_{\tau-\Delta\tau/2}^{\tau+\Delta\tau/2} \int_{-L_y/2}^{+L_y/2} n(x, y, t) dy dt. \quad (17)$$

We will assume that blobs (or fronts) are created at a uniform rate at $x=0$ such that on average there are M_b blobs per unit area in the (x, y) plane. Then the integrals in Eq. (17) will be over $M_b L_y V_x(\tau) \Delta\tau$ number of blobs. Thus, they can be replaced by the following integrals over the blob density given in Eq. (16):

$$\bar{n}[X(\tau)] = M_b V_x(\tau) \int_{-\infty}^{+\infty} \int_{-\infty}^{+\infty} n(\xi, y, \tau) d\xi dy, \quad (18)$$

which leads to (in the comoving frame)

$$\bar{n}[X(\tau)] = C \frac{\exp(-\alpha\tau)}{\tau + \tau_D}, \quad (19)$$

where $C = C(\alpha, \beta, D, M_b, n_b)$ is some constant and $\tau_D \equiv a_0^2/(4D)$ is the blob diffusion time. Solving for τ using the definition of $X(\tau)$ given above, we get

$$\tau = \tau_D [\exp(X/\lambda_D) - 1], \quad (20)$$

where $\lambda_D = \beta/(2\alpha D) \approx V_x \tau_D$ is a more precise form of the hybrid length scale that we called a_D in Eq. (11). Substituting for τ in Eq. (19) finally leads to the mean density profile (in the laboratory frame)

$$\bar{n}(x) = n_0 \exp(-x/\lambda_D) \exp\left[-\frac{\tau_D}{\tau_\alpha} [\exp(x/\lambda_D) - 1]\right], \quad (21)$$

where $\tau_\alpha \equiv 1/\alpha$, and we introduced a new constant n_0 .

Up to this point, we essentially made no approximations. Before we move on to comparisons with numerical results below, we will point out two distinct limits. Because of the appearance of the term $\exp(x/\lambda_D)$ within an exponential in Eq. (21), it is clear that λ_D defines an approximate upper limit on the density width in the SOL. For $\beta/\alpha=5$ and $D = 1.0 \times 10^{-3}$ ($D \approx 0.1$ m²/s), we have $\lambda_D = 2.5 \times 10^3 \rho_s \approx 5$ m for NSTX, a length scale that is physically irrelevant, and $\lambda_D \approx 4$ cm for “high-field” C-Mod, using parameters from Ref. 2. Thus, assuming $x \leq \lambda_D$ and letting $[\exp(x/\lambda_D) - 1] \rightarrow (x/\lambda_D)$, we get

$$\bar{n}(x) \approx n_0 \exp[-x(1 + \tau_D/\tau_\alpha)/\lambda_D]. \quad (22)$$

Then for $\tau_D/\tau_\alpha \ll 1$, we have

$$\bar{n}(x) \approx \exp(-x/\lambda_D). \quad (23)$$

Thus in this limit the density length scale is $\lambda_n \approx \lambda_D$, implying essentially a flat profile. Note that $\lambda_D \sim R^0$, i.e., it is independent of the machine size. (However, $\lambda_n \sim R^0$ only in the limit $\alpha/D \rightarrow 0$. For finite α/D , $\lambda_n \sim R^\nu$, with $\nu < 1/2$.) In the opposite limit, $\tau_D/\tau_\alpha \gg 1$, we get

$$\bar{n}(x) \approx \exp\left[-\frac{x}{(\lambda_D \tau_\alpha / \tau_D)}\right], \quad (24)$$

giving $\lambda_n = \lambda_D (\tau_\alpha / \tau_D) \ll \lambda_D$. For constant β/α , we have the scaling $\lambda_n \sim R^{1/2}$ in this limit. Recall that in the absence of convection, the purely diffusive length scale is $\lambda_{\text{diff}} = (D/\alpha)^{1/2}$, which also scales as $R^{1/2}$. However, λ_{diff} is obvi-

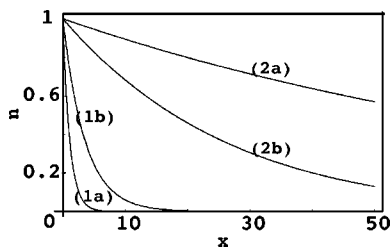


FIG. 10. Comparison of purely diffusive profiles [1(a) and 1(b)] with convective profiles from Eq. (21) [2(a) and 2(b)] using NSTX-like parameters: $\alpha = 8 \times 10^{-4}$, $\beta = 4.7 \times 10^{-3}$. In both cases $D = 1.0 \times 10^{-3}$ ($D = 0.1 \text{ m}^2/\text{s}$) for (a) and $D = 1.0 \times 10^{-2}$ ($D = 1 \text{ m}^2/\text{s}$) for (b). The horizontal axis is in units of ρ_s (2 mm here).

ously much shorter than $\lambda_n = \lambda_D(\tau_\alpha/\tau_D)$ for $D \ll \alpha$. (Note that all variables without units in this discussion are by default normalized, i.e., dimensionless.)

Purely diffusive and convective profiles are compared in Fig. 10 for NSTX-like parameters. Using $\rho_s = 2 \text{ mm}$, $L = 5 \text{ m}$, $\Omega_i = 2.4 \times 10^7/\text{s}$, $\bar{n}(x)$ from Eq. (21) and $n(x) = \exp(-x/\lambda_{\text{diff}})$ are plotted for two different values of diffusivity, $D = 0.1 \text{ m}^2/\text{s}$ and $D = 1 \text{ m}^2/\text{s}$. As expected, the purely diffusive profiles broaden with increasing D [Fig. 10, (1a) \rightarrow (1b)], whereas the convective profiles get narrower [Fig. 10, (2a) \rightarrow (2a)] because of the flattening and slowing down of the fronts with higher diffusivity.

In order to simplify the arguments, the discussion in this section was kept in an “initial-value” form and influences of boundary conditions were ignored. In Appendix A, possible effects of boundary conditions at the separatrix and their role in the “two-layer” SOL profiles²¹ are explored.

Next we turn to a comparison of some of the results of this section with nonlinear numerical calculations.

A. Comparison with turbulence calculations

As by Ghendrih *et al.*,¹³ we examine the mean-density profiles in two-dimensional SOL interchange-mode turbulence driven by a constant source term at the separatrix ($x = 0$); Eq. (2) is modified to include on the right-hand-side a term $S_0[1 + \epsilon(x, y)]\exp[-(x/w_s)^2]$, where S_0 is a constant amplitude, $\epsilon(x, y)$ is a small random component ($\epsilon \ll 1$), and $w_s \sim (2-4)\rho_s$ is the source width. Thus, the turbulence here will be “flux-driven”,²² with its intimate connections to the concepts of self-organized criticality and “avalanches”.²³ Our scaling studies differ from that of Ghendrih *et al.* in one important respect: instead of varying only the parallel loss term, we vary both the curvature drive and the loss terms in Eqs. (1) and (2), keeping the ratio β/α constant.

Figure 11 summarizes the scaling of λ_n with α , which is inversely related to the machine size R through $\alpha = 2\rho_s/(qR)$, in two different parameter regimes referred to in the preceding section. In Fig. 11(a), the blob or front diffusion time is shorter than the decay time due to parallel losses. In this set of calculations, a grid size of $\Delta x = \Delta y = \rho_s$ was used, with typically 512×512 points. As mentioned earlier, the initial blob size is assumed to be determined by the most unstable mode, to within a constant of order unity, chosen to agree with the numerical results at one point. Here, we let

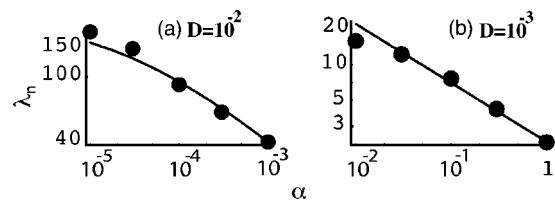


FIG. 11. Scaling of λ_n , the density scale length in the SOL, with $\alpha = 2\rho_s/L$, in two different parameter regimes. The solid lines are from the analytic solution, Eq. (21). The points are numerical results. (a) $D \gg \alpha$, diffusion dominated; (b) $D \ll \alpha$, parallel-loss dominated. The ratio β/α is held fixed at $\beta/\alpha = 5$.

$a_0 = 1.3 \times \lambda_{\text{linear}}$ to ensure the point at $\alpha = 10^{-3}$ is on the analytic curve. With this caveat, the numerical results are in good agreement with our earlier analytic results. The point at $\alpha = 10^{-5}$ required a 768×512 mesh, and the calculation had to be run for $t > 4 \times 10^5 \Omega_i^{-1}$ units of time. It is possible that it needed to be continued further to bring the point closer to the analytic curve. As expected, in this regime, λ_n does not scale with R^ν with a constant ν , although the error bars on the points do not rule out $\nu = 1/3$ of Ref. 4. Note that, under similar conditions, Ghendrih *et al.* would predict the scaling $\lambda_n \sim R^{1/8}$.

In the opposite (but less physical) limit $D \ll \alpha$ where the parallel losses dominate, the scaling is approximately $\lambda_n \sim \alpha^{-1/2}$, as seen in Fig. 11(b). Since $a_0 \sim \lambda_{\text{lin}} = 2\pi(D/\alpha)^{1/4} \sim \rho_s$ here, a much finer grid had to be used for this set of calculations, with $\Delta x = \Delta y \leq (1/8)\rho_s$, still typically using a 512×512 mesh. Note that the connection length implied by these values of the parameter α ($L \sim \rho_s$ for $\alpha = 1$) is obviously not physical; however, keeping α in a physically relevant range while maintaining the inequality $D \ll \alpha$ requires values of particle diffusivity that is not computationally feasible.

Despite the lack of relevance of this parameter regime, we briefly mention in Appendix B a result obtained under these conditions that may have more generality: spontaneously generated “spinning blobs” with a predominantly monopolar potential field.

VI. SUMMARY AND CONCLUSIONS

Blobs are thought to be responsible for convective and intermittent transport in the scrape-off layer of tokamaks. In this work we discussed a number of issues related to their creation and dynamics. Revisiting and enlarging upon some of the earlier works, we showed the following.

- (1) Within the symmetries of the problem, the analytic solution found by Krasheninnikov of the nonlinear model equations is actually a unique solution consistent with the assumptions of a traveling wave. The inertia term vanishes identically, without requiring it as an *a priori* assumption, and there are no other solutions that somehow include finite inertia.
- (2) Numerical solutions, however, differ significantly from a simple traveling wave. In addition to having a significant contribution from inertia, they are also more like 2D versions of the shock-wave solutions of the Burgers’

equation, with a steepened leading edge and a long tail. Thus, dissipation in the system plays an inherently important role in blob dynamics.

- (3) An important consequence is that whether a blob propagates as a coherent structure depends on the dissipation level in the system, in addition to the size of the blob. For dissipation levels on the order of $\mu=D=0.1 \text{ m}^2/\text{s}$, and for a typical set of dimensionless parameters α, β , we find no coherent behavior, regardless of the size. Small blobs, affected by inertia, are unstable to Kelvin–Helmholtz modes. They essentially disintegrate by vortex shedding. As the size increases, vortices give way to interchange mode-driven fingers, which again destroy the blobs.
- (4) When the blob size is greater than the inertial length scale, $\delta_b \geq a_m$, coherence emerges as dissipation is increased. It may be useful to determine the boundaries of coherent behavior in, for example, δ_b vs D plane, as a function of β/α . However, we expect these dynamical details to be modified with the inclusion of more physics in the simple model used here, and we will defer that calculation to a future paper.
- (5) Again including dissipation as an important part of the discussion, we discussed linear and nonlinear interchange stabilities in the SOL. We showed how the fingers driven by the SOL interchange mode transform nonlinearly into blobs as they propagate radially.
- (6) Using a localized Gaussian perturbation of a typical SOL density profile, we showed the formation of a cascade of blobs that essentially carry all the mass to the wall and evacuate the region outside the separatrix.
- (7) Finally, we presented a simple model of how the convective transport in the SOL may lead to a mean density profile that is in qualitative agreement with experimental observations. Our model makes somewhat different predictions from previous work on this topic; although it is supported by our numerical calculations, computational difficulties (mainly required computer time) prevent us from making definitive statements.
- (8) We also demonstrated an unanticipated formation of monopolar (spinning) blobs within our two-field model, which we intend to examine in some detail in the near future.

ACKNOWLEDGMENTS

The author acknowledges a useful discussion with P. J. Morrison, J. Van Dam, and F. L. Waelbroeck on the analytic solutions of the model equations.

This work was supported by the U.S. Department of Energy under Contract No. DE-FG03-96ER-54346.

APPENDIX A

Here we briefly discuss the role of boundary conditions in determining the SOL density profiles in terms of the following 1D transport equation for the mean density (averaged over the poloidal direction):

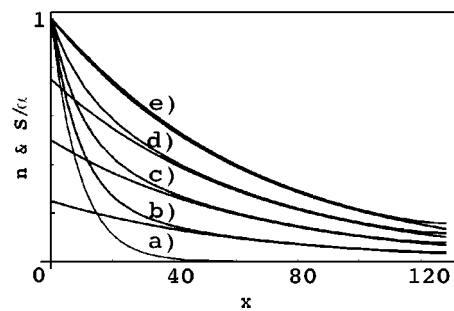


FIG. 12. Density and source function profiles as the source strength is varied. All density profiles have $n(0)=1$. The remaining curves show $S(x)/\alpha$, where $S(x)$ is the particle source function. (a) $S_0=0$, (b) $S_0/\alpha=0.25$, (c) $S_0/\alpha=0.5$, (d) $S_0/\alpha=0.75$, (e) $S_0/\alpha=1$. Note that, except for a layer of width $1/k_D$ near the separatrix ($x=0$), the density profiles closely follow $S(x)/\alpha$. For $S_0/\alpha=1$ [curve (e)], $n(x)$ and $S(x)/\alpha$ curves overlay each other within the accuracy of the plot. The inverse diffusion length $k_D=0.28$ for all cases shown here.

$$\frac{\partial n}{\partial t} + \frac{\partial \Gamma_{\perp}}{\partial x} = -\alpha n + D \frac{\partial^2 n}{\partial x^2}, \quad (\text{A1})$$

where $\Gamma_{\perp} \equiv \langle \bar{n} \bar{v}_x \rangle$, and the brackets, which are implied for the mean density n , denote the y average. Assuming constant coefficients α, D , and using the boundary conditions $n(x)=n_0$ at $x=0$, the separatrix, and $\partial n/\partial x=0$ at $x=L_x$, the outer boundary, a general steady-state solution can be written in the form

$$\begin{aligned} n(x) = & n_0 \frac{\cosh[k_D(x-L_x)]}{\cosh(k_D L_x)} + \frac{1}{k_D D \cosh(k_D L_x)} \\ & \times \int_0^x S(\xi) \cosh[k_D(x-L_x)] \sinh(k_D \xi) d\xi \\ & + \frac{1}{k_D D \cosh(k_D L_x)} \\ & \times \int_x^{L_x} S(\xi) \cosh[k_D(\xi-L_x)] \sinh(k_D x) d\xi, \quad (\text{A2}) \end{aligned}$$

where we replaced the particle flux term with a general source, $S(x) \equiv -\partial \Gamma_{\perp} / \partial x$, and defined the inverse diffusion length $k_D \equiv \lambda_{\text{diff}}^{-1} = \sqrt{\alpha/D}$.

We analyze the effects of the particle flux term in Eq. (A2) in general terms by assuming a source of the form $S(x) \equiv \partial \Gamma_{\perp} / \partial x = S_0 \cosh[k_D(x-L_x)/L_S] / \cosh(k_D L_x / L_S)$, where L_S is a length scale we arbitrarily take to be $L_x/2$ here. (Note that this functional form is convenient but not necessary for the general conclusions we will draw below.) The density profiles obtained with various source amplitudes for fixed $k_D=0.28$ are shown in Fig. 12. All curves exhibit two important characteristics. (i) Nearly for all S_0 , there is a “boundary layer” at $x \approx 0$ of width $1/k_D = (D/\alpha)^{1/2}$. [If we use the boundary condition $n(x=L_x)=0$ at the wall, we get a similar layer at $x \approx L_x$ in which $n(x) \rightarrow 0$.] (ii) Outside this layer, the density profile is determined by the source $S(x)$: $n(x) \approx S(x)/\alpha$. Of course, these observations also follow from Eq. (A2): within the boundary layer, $D \partial^2 n / \partial x^2 \approx \alpha n$; outside, we simply have $\alpha n(x) \approx S(x)$.

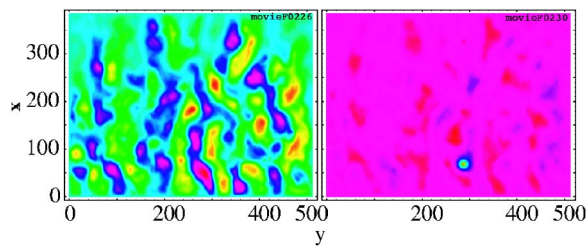


FIG. 13. The potential ϕ just before and after a spinning blob is formed for $D=1.0 \times 10^{-3}$, $\alpha=3 \times 10^{-2}$, and $\beta=1.5 \times 10^{-1}$.

From this simple analysis, a possible explanation for the “two-layer” structure of the SOL density profiles²¹ emerges. Near the separatrix, a balance between parallel losses and perpendicular diffusion gives rise to a layer of steep exponential decay with an e -folding length of $\lambda_{\text{diff}} \approx (D/\alpha)^{1/2}$. In fact, with a knowledge of this length scale, one can determine the diffusivity near the separatrix using an estimate for $\alpha=2c_s/L$ (in dimensional units). For $x > \lambda_{\text{diff}}$, the balance is between the convective particle flux and parallel losses, and the length scale is determined by $S(x)=-\partial\Gamma_{\perp}/\partial x$, which can be quite different from λ_{diff} . (As we saw earlier, the flux itself can be affected by D , which is a separate issue.) Note that as the source amplitude increases, the boundary layer shrinks and the two-layer structure gradually disappears, in qualitative agreement with experimental observations²¹ under high-density (and presumably high particle flux) conditions.

APPENDIX B

Blobs or fronts considered in the main body of this work all have a dipole potential field associated with them that help convect them radially. In the flux-driven turbulence calculations, under poorly understood conditions, we also observe blob formations that have a strong monopolar potential. These structures are seen in three-field models that allow for a temperature gradient across the blob (spinning blobs), and their properties have been studied in a recent work by Myra *et al.*⁹ However, since we have ignored all temperature gradients in this work, their spontaneous appearance in some of our calculations is a surprise. While we intend to study this phenomenon in some detail in a future work, we present here an example of their time history. Figure 13 shows the potential field just before and after the formation of a spinning blob. The dipolar structure of the field associated with elongated convection cells is apparent in the first panel. The second one, however, is obviously dominated by a monopole. Slow propagation and eventual decay of the blob itself is shown in Fig. 14, where it is highlighted with a circle.

It is already clear that dissipation plays a somewhat different role for these spinners than it does in the dipolar ones. In the latter, in general some dissipation is necessary for stability, whereas the spin seems to provide the required sta-

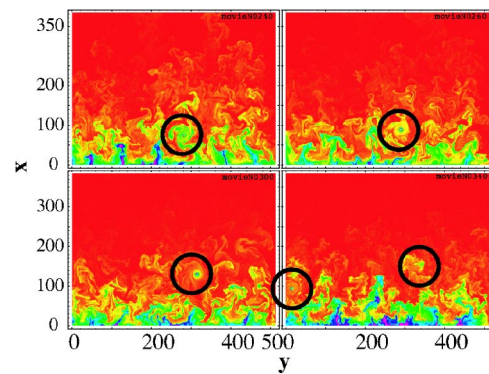


FIG. 14. Particle density, showing the evolution of a spontaneously generated spinning blob (circled). Note that the last frame shows the birth of a new one at the lower left as the old one decays.

bility for the former, and perpendicular diffusion or parallel losses seems to merely control the decay rate.

- ¹V. I. Pistunovich, in *Plasma Physics and the Problem of Controlled Thermonuclear Reactions*, edited by M. A. Leontovich (Pergamon, New York, 1961), Vol. 4, p. 1.
- ²J. L. Terry, S. J. Zweben, K. Hallatschek, B. LaBombard, R. J. Maqueda, B. Bai, C. J. Boswell, M. Greenwald, D. Kopen, W. M. Nevins *et al.*, *Phys. Plasmas* **10**, 1739 (2003).
- ³S. I. Krasheninnikov, *Phys. Lett. A* **283**, 368 (2001).
- ⁴D. A. D'Ippolito, J. R. Myra, and S. I. Krasheninnikov, *Phys. Plasmas* **9**, 222 (2002).
- ⁵N. Bian, S. Benkadda, and J.-V. Paulsen, *Phys. Plasmas* **10**, 671 (2003).
- ⁶G. Q. Yu and S. I. Krasheninnikov, *Phys. Plasmas* **10**, 4413 (2003).
- ⁷D. A. D'Ippolito and J. R. Myra, *Phys. Plasmas* **10**, 4029 (2003).
- ⁸O. Garcia, V. Naulin, A. H. Nielson, and J. J. Rasmussen, *Phys. Rev. Lett.* **92**, 165003 (2004).
- ⁹J. R. Myra, D. A. Dippolito, S. I. Krasheninnikov, and G. Q. Yu, *Phys. Plasmas* **11**, 4267 (2004).
- ¹⁰G. F. Carrier and C. E. Pearson, *Partial Differential Equations* (Academic, New York, NY, 1976).
- ¹¹A. V. Nedospasov, *Sov. J. Plasma Phys.* **15**, 659 (1989).
- ¹²X. Garbet, L. Laurent, J.-P. Roubin, and A. Samain, *Nucl. Fusion* **31**, 867 (1991).
- ¹³P. Ghendrih, P. Kaw, Y. Sarazin, P. Beyer, S. Benkadda, G. Falchetto, X. Garbet, V. Grandgirard, and M. Ottaviani, *Proceedings of the 20th IAEA Fusion Energy Conference*, edited by the IAEA Editorial staff, Vilamoura, Portugal, Nov. 2004.
- ¹⁴Y. Sarazin and P. Ghendrih, *Phys. Plasmas* **5**, 4214 (1998).
- ¹⁵H. R. Strauss, *Phys. Fluids* **20**, 1354 (1977).
- ¹⁶S. Chandrasekhar, *Hydrodynamic and Hydromagnetic Stability* (Oxford University Press, Oxford, 1961).
- ¹⁷H. L. Berk, D. D. Ryutov, and Y. A. Tsidulko, *Phys. Fluids B* **3**, 1346 (1991).
- ¹⁸H. L. Berk, R. H. Cohen, D. D. Ryutov, Y. A. Tsidulko, and X. Q. Xu, *Nucl. Fusion* **33**, 263 (1993).
- ¹⁹S. V. Novakovskii, P. N. Guzdar, J. F. Drake, and C. S. Liu, *Phys. Plasmas* **2**, 3764 (1995).
- ²⁰W. Kerner, A. Nassigh, and O. Pogutse, *Plasma Phys. Controlled Fusion* **39**, 1101 (1997).
- ²¹B. LaBombard, R. L. Boivin, M. Greenwald, J. Hughes, B. Lipschultz, D. Mossessian, C. S. Pitcher, J. L. Terry, S. J. Zweben, and A. Group, *Phys. Plasmas* **8**, 2107 (2001).
- ²²X. Garbet and R. Waltz, *Phys. Plasmas* **5**, 2836 (1998).
- ²³P. H. Diamond and T. S. Hahn, *Phys. Plasmas* **2**, 3640 (1995).